

MICROWAVE PHOTONIC INTERFERENCE
CANCELLATION: RF ANALYSIS, III-V AND SILICON
INTEGRATION, DEVELOPMENT OF BALANCED AND
HYBRID ARCHITECTURES

ERIC CHARLES BLOW

A DISSERTATION
PRESENTED TO THE FACULTY
OF PRINCETON UNIVERSITY
IN CANDIDACY FOR THE DEGREE
OF DOCTOR OF PHILOSOPHY

RECOMMENDED FOR ACCEPTANCE
BY THE DEPARTMENT OF
ELECTRICAL AND COMPUTER ENGINEERING
ADVISOR: PROFESSOR PAUL R. PRUCNAL

JANUARY 2024

Contents

| | |
|---|----------|
| Abstract | iii |
| List of Tables | vi |
| List of Figures | vii |
| 1 RF Performance Analysis of Microwave Photonic Cancellation | 1 |
| 1.1 Generalized Microwave Photonic Link | 1 |
| 1.2 Link Gain/Loss of Microwave Photonic Link | 4 |
| 1.3 Noise Figure of Microwave Photonic Link | 10 |
| 1.4 Preamplification of Microwave Photonic Link | 17 |
| 1.5 Silicon Photonic Loss Mechanisms | 19 |
| 1.5.1 Linear and Nonlinear Waveguide Loss | 20 |
| 1.5.2 Nonlinear Microring Resonator Loss | 24 |
| 1.6 Spurious-Free Dynamic Range | 27 |

List of Tables

List of Figures

| | | |
|------|---|----|
| 1.1 | Generalized microwave photonic link with an intensity modulation direct detection (IMDD) architecture. | 2 |
| 1.2 | Link loss of intensity modulated direct detection link. | 5 |
| 1.3 | Direct and external modulation transfer functions. | 6 |
| 1.4 | Simulated link loss verse optical power for discrete directly modulated link. | 7 |
| 1.5 | Simulated link loss verse optical power for discrete externally modulated link. | 8 |
| 1.6 | Example RIN frequency spectrum for commercial laser. | 12 |
| 1.7 | Noise figure verse optical power simulation for standard directly modulated and externally modulated links. | 14 |
| 1.8 | Highlighting different noise regions by analyzing derivative of noise figure as function of optical power. | 15 |
| 1.9 | Noise figure verse optical power of a standard EM link while sweeping RIN. | 16 |
| 1.10 | Noise figure verse optical power of a standard DM link while sweeping RIN. | 16 |
| 1.11 | Noise figure analysis with the inclusion of low noise amplification. | 18 |
| 1.12 | Noise figure analysis with the inclusion of low noise amplification while sweep LNA gain. | 18 |
| 1.13 | Noise figure analysis with the inclusion of low noise amplification while sweep LNA noise figure. | 19 |
| 1.14 | Optical power within the waveguide as a function of distance within the waveguide for varying optical powers. | 23 |

| | | |
|------|--|----|
| 1.15 | Link loss and noise figure analysis for EM and DM links considering silicon photonic waveguide loss. | 23 |
| 1.16 | Power buildup within a microring resonator (MRR) as function of detuning | 24 |
| 1.17 | Optical power as a function of waveguide distances for varying optical powers within a 15 micron radius microring resonator | 25 |
| 1.18 | Optical linear and nonlinear loss of 15 micron microring with varying buildup factor. | 25 |
| 1.19 | Link loss and noise figure as a function of optical input power for both DM and EM silicon photonic links with a 15 micron radius microring resonator. | 26 |
| 1.20 | Link loss and noise figure as a function of input optical power for a silicon photonic circuit with microring resonators with sweeping buildup factors. | 27 |
| 1.21 | Graphical representation of spurious-free dynamic range. | 29 |
| 1.22 | SFDR of directly modulated and externally modulated silicon photonic link with nonlinear loss as a function of optical power. | 30 |
| 1.23 | SFDR of directly modulated and externally modulated silicon photonic link as a function of optical power while sweeping the buildup factor of an MRR from 4.3 to 40. | 31 |
| 1.24 | SFDR of DM and EM silicon photonic links with microring resonators as a function of optical power with sweeping low noise amplification gain. | 31 |
| 1.25 | SFDR of DM and EM silicon photonic links with microring resonators as a function of optical power with sweeping low noise amplification noise figure. | 32 |

Chapter 1

RF Performance Analysis of Microwave Photonic Cancellation

In comparison with traditional technological platforms, such as RF analog and digital processing, microwave photonic processors offer an GHz of instantaneous bandwidths and 10 GHz of tunability. The caveat of microwave photonics, often not addressed in the literature, is the RF performance of these systems. Within this chapter, RF analysis techniques will be presented for discrete microwave photonic systems and then extended specifically to a silicon microwave photonic platform. The performance trade-offs between key device parameters will be explored and simulated. Additionally, the performance improvement and degradation due to silicon photonic integration will be presented. Specifically, the effect on performance due to the nonlinear loss mechanisms in silicon photonic waveguides and ring resonators. This chapter was developed as an extension to the theory presented in the following primary references: [1, 2, 3, 4, 5, 6, 7, 8]. Source code for the simulations within this chapter is available online: https://github.com/ericcblow/MWP_RF_Sims

1.1 Generalized Microwave Photonic Link

The microwave photonic system to be analyzed within this chapter is shown in a generalized form in Fig. 1.1. Microwave photonic processing begins with the up-conversion of a high-speed optical signal onto a coherent optical carrier. Current microwave photonic systems operate within the optical O-Band, wavelengths 1260-1360 nm, and the C-Band, wavelengths 1530–1565 nm.

Both bands are transparency windows for silica-based fibers and waveguides. The O-Band is the spectral region with the lowest chromatic dispersion [9]. The C-Band is the spectral region with lowest loss and, therefore, is ubiquitous within telecommunication networks. Within the analysis and research presented in this thesis, a 1550 nm, 193 THz, C-Band laser source was implemented. The analysis presented within this chapter limits the up-conversion technique to intensity modulation.

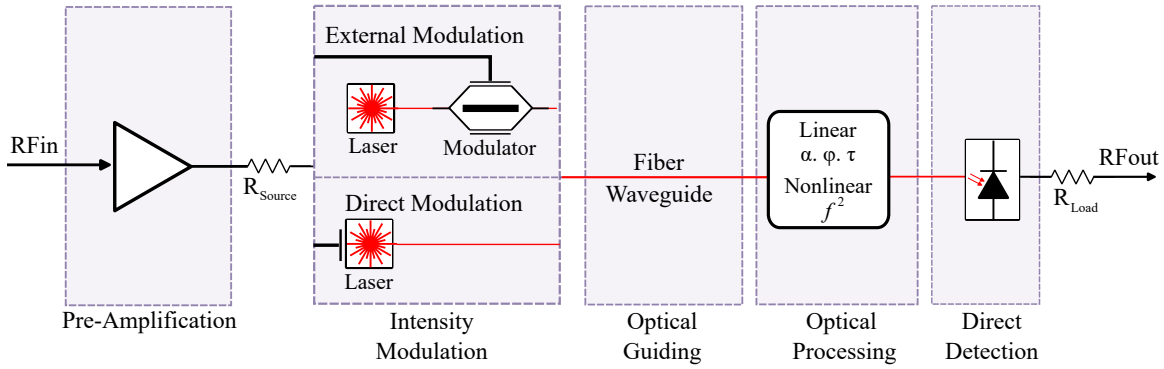


Figure 1.1: Generalized microwave photonic link with an intensity modulation direct detection (IMDD) architecture.

Intensity modulation can be accomplished by direct modulation of the laser source or external modulation of the optical carrier, Fig. 1.1. Primary methods of external intensity modulation include interferometric, such as Mach-Zehnder Modulators (MZMs) and Michelson interferometric modulators (MIMs), as well as electro-absorption modulators. Externally modulated links have become increasingly more popular compared to directly modulated lasers due to higher bandwidths and the overall high performance of bulk Lithium Niobate modulators [1]. In recent years, the speed of research-grade directly modulated lasers has increased upwards of 65 GHz [10].

Following the modulation of the RF signal onto the optical carrier, the microwave photonic system requires guiding. Guiding light is a complex field in its own right. Optical modes must be matched from device to device across technological platforms. This can be particularly challenging when coupling fiber-based optical components to an integrated photonic chip [11]. Changing materials leads to interfaces with differing refractive indices. This leads to Fresnel reflections equal to eqn. 1.1 at normal incidence [9]. This optical reflection can only be mitigated through monolithic

photonic integration. Additionally, many optical devices are polarization dependent. Therefore, polarization must be maintained or corrected throughout the microwave photonic system.

$$R = \left(\frac{n_1 - n_2}{n_1 + n_2} \right)^2 \quad (1.1)$$

As discussed within the introduction, a tunable optical processing element can enable 10s of GHz of broadband processing [12]. This is due to the small relative bandwidth of the modulated RF signal compared to the 193 THz of the optical carrier. For example, dynamic optical switching can offer a flat weighting of many wavelength signals simultaneously [13]. For example, an optical device exhibits a flat processing response over the optical C-Band, translating to having a 3.7 THz processing bandwidth. While this is an extreme example, wavelength division multiplexed (WDM) microwave photonic processing often offers 10-100 GHz in RF processing bandwidths [14, 15].

Unlike in CMOS analog electronics, microwave photonic processing does not have a fundamental processing element, such as the transistor, which is implemented in different orientations and configurations to achieve a unique processing task. In photonics, separate processing tasks require unique optical solutions. Optical processing, whether linear or non-linear, will contribute to the RF performance of the systems with respect to signal power and noise power.

Lastly, the processed modulated optical signal must be down-converted back to the electrical domain. The RF analysis and system presented in this thesis focus on incoherent optical links and direct detection. Therefore, the optical links studied within this chapter are known as intensity-modulated direct-detection (IM-DD) [16]. An alternative link architecture would be coherently combine the processed optical signal with a local oscillator, performing optical heterodyning. Then the down-converted signal is detected with a photodetector [17]. There are trade-offs present between bandwidths and down-conversion efficiencies between these two architectures. In recent years, coherent microwave photonic cancellation has also been explored [18, 19]. Within optical-to-electrical conversion, additional processing capabilities can be realized, such as WDM summation and subtraction.

1.2 Link Gain/Loss of Microwave Photonic Link

The link gain (Gain > 1 dB) or link loss (Gain < 1 dB) is the change in RF power transmission through an RF link. With respect to microwave photonic systems, these systems are traditionally lossy and therefore link loss is the most commonly used term [16]. The link loss is defined as the power ratio between the input and output of the device-under-test. As defined by network theory [20, 21], the source power and the load power can be further defined by the temporal average of the source voltage, V_S , the current flowing through the load, I_L , as well as the source and load resistance, R_S and R_L . With respect to microwave photonic links, V_S is analogous to the voltage driving the modulator and I_L is analogous to the generated photocurrent. Eqn. 1.2 provides insights to the impact of impedance matching on the microwave photonic link. In the research and analysis presented within this thesis, resistive matching, a lossy impedance matching, is deployed ($R_S = R_L = 50\Omega$). This results in a factor of 1/4 or 6 dB signal reduction, but does not limit the frequency response of the system as such with active impedance matching. While not considered in this work, impedance matching can significantly improve the RF performance of a microwave photonic system over limited frequency ranges [22].

$$G_{RF} = \frac{P_{out}}{P_{in}} = \frac{I_L^2 R_L}{V_S^2 / 4R_S} \quad (1.2)$$

To calculate the link loss of a discrete microwave photonic system (eqn. 1.3), one must account for the electrical-optical-electrical (E-O-E) conversion efficiencies, G_{Mod} and G_{Detect} , the gain of impedance matching, $G_{Impedance}$, and the optical gain due to optical guiding and processing, G_{opt} . A typical S21 measurement of link gain for a microwave photonic link, shown in Fig. 1.2, highlights modulation bandwidth dependency as well as typical RF reflections due to lossy impedance matching.

$$G_{RF} = (G_{Impedance})^2 (G_{Mod})^2 (G_{Opt})^2 (G_{Detect})^2 \quad (1.3)$$

Modulation Efficiency: There are two primary modulation types for microwave pho-

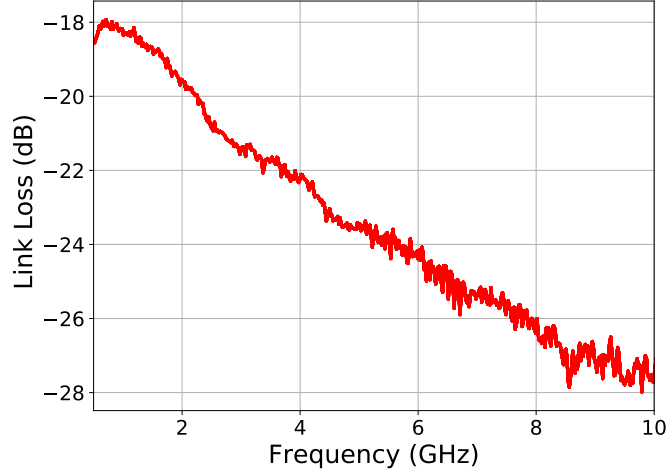


Figure 1.2: Link loss of intensity modulated direct detection link. Example data from optical link with microwave photonic canceller.

tonic links: direct modulation and external modulation. In a direct modulation architecture, the RF power into the microwave photonic system directly drives the laser source 1.3. The directly modulated laser (DML) simplifies the circuit by acting as the optical source and modulation device. Fig. 1.3 (left) shows the light-current (LI) curve of a laser diode. The device requires a threshold current, I_{th} to achieve population inversion and begin lasing [9]. Following the threshold current, the injection current linearly results in optical power generation. The efficiency of this conversion is defined by the quantum efficiency of the material [1, 9]. The slope efficiency, s_{LD} , of the laser diode is the slope of the linear region of the DML transfer function. At $1.3 \mu m$ the theoretical maximum slope efficiency is $0.95 W/A$ with a differential quantum efficiency, n_d , of 100 % [23].

$$P_{LD}(t) = s_{LD}(I_{LD}(t) - I_{th}) \quad (1.4)$$

In a directly modulated link, the change in optical power is directly proportional to the change in injection current, and therefore the RF gain due to direct modulation is equal to the square of the slope efficiency, eqn. 1.51.5. The link loss for a typical directly modulated microwave photonic link was simulated in Fig. 1.4. The optical loss, defined as 5 dB, and a responsivity of $0.75 A/W$. The slope efficiency was varied from the slope efficiency of a vertically-coupled

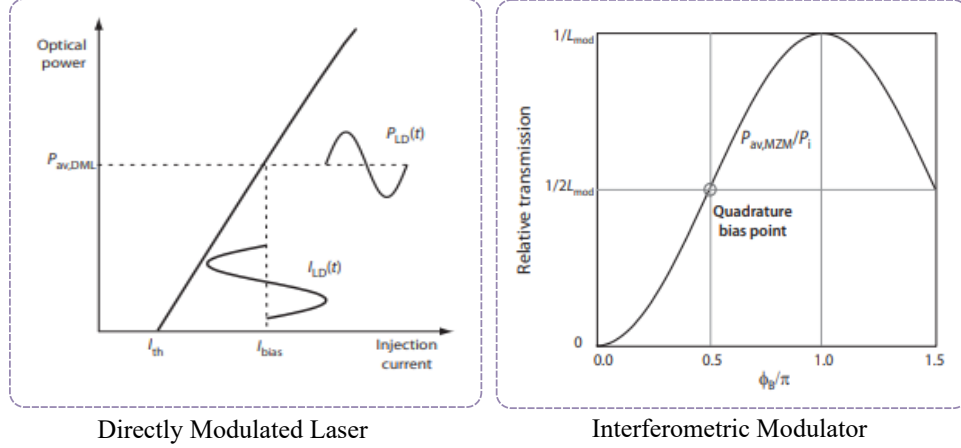


Figure 1.3: Directly modulated laser transfer function (left), showing optical power out of optical source as function of injection current. Externally modulated interferometric transfer function (right). Relative optical transmission as function of applied voltage [21]

surface emitting laser (VCSEL) 0.06514 mW/mA [24] to that of a laser diode with high-order slotted surface gratings, 0.4 mW/mA , specifically optimized for slope efficiency [25]. The low s_{LD} VCSEL, results in a link loss of -42.76 dB while the high s_{LD} , results in a link loss of -26.48 dB . For reference, a typical commercial-of-the-shelf (COTS) directly modulated laser can be expected to have a slope efficiency of 0.3 mW/mA [26].

Note that given this linear approximate, the link loss of direct modulation is independent of optical power. In practice, the slope of the laser will vary resulting in nonlinearities, which will be further discussed within the spurious-free dynamic range section.

$$G_{DMmod} = (s_{LD}) \quad (1.5)$$

Alternatively, a modulator may be placed in series with the laser source to attenuate the optical power of the CW optical source. Typically, an interferometric modulator, such as a Mach-Zehnder Modulator (MZM), or an Electro-Absorption Modulator (EAM) is used. An interferometric modulator can be modeled by a raised cosine transfer function [9], shown in Fig. 1.3 (right). The applied voltage, defined here as the half-wave voltage divided by π , applies a phase shift in one arm of the interferometer via the Pockel effect [9]. The half-wave, π , voltage is the required

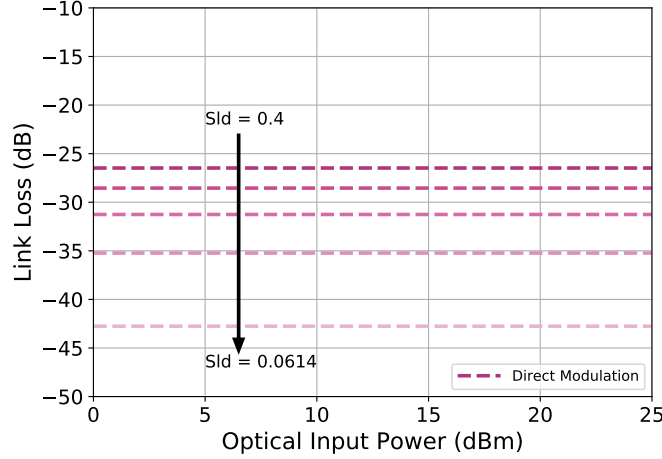


Figure 1.4: Simulated link loss verse optical power for discrete directly modulated link with 5 dB optical loss and a 0.75 A/W responsivity. Slope efficiency varying from 0.06514 mW/mA [24] to 0.4 mW/mA [25]

voltage to swing the modulator from full transmission to zero transmission. This required voltage is the sensitivity of the modulator. The quadrature bias point is half of the V_π and is the point of highest slope. Similarly to the directly modulated link, the slope of the modulation transfer function is proportional to the efficiency of modulation. The transfer function of an EAM is governed by the Franz-Keldysh effect for bulk semiconductors and the Quantum-Confined Stark Effect, for quantum well materials [9, 6]. The negative slope of an EAM transfer function can be mapped to the raised cosine transfer function of the interferometric modulators. This fit results in an effective V_π .

Unlike direct modulation, there are multiple metrics which impact the gain of the conversion other than the slope of the modulation. The insertion loss introduced by the modulator, T_{mod} , will also degrade the conversion efficiency [1]. The amount of optical power into the external modulator will effectively stretch the transfer function, resulting in a slope dependence on the optical power into the modulator. Lastly, the efficiency of an external modulator will depend on the load resistance, R_L .

$$G_{EMmod} = \left(\frac{P_{opt} T_{Mod} R_L \pi}{2V_\pi} \right) \quad (1.6)$$

A typical externally modulated link was simulated and as shown in Fig. 1.5. A standard externally modulated link with 5 dB optical loss, 50Ω load resistance, and a $0.75 A/W$ responsivity. The V_π was varied from a highly sensitive integrated 1 V, representing a 2 mm long BaTiO₃-based electro-optic Pockels modulator [27], to 14.4 V representing a highly compact, 500 μm , silicon pn-junction MIM [28]. At a standard optical operating point of 15 dBm, the link loss for the low sensitivity modulator and high sensitivity modulator was -42 dB and -19 dB respectively. Note, the transmission loss, T_{mod} , was kept fixed at 4 dB for both modulators to highlight only the effect of sweeping sensitivity.

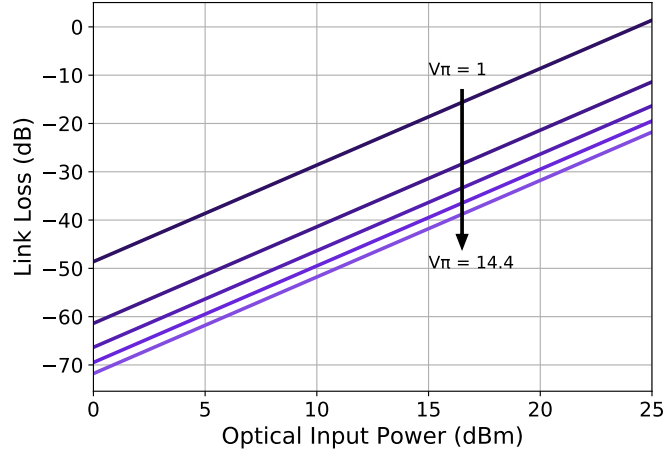


Figure 1.5: Simulated link loss verse optical power for discrete externally modulated link with 5 dB optical loss and a $0.75 A/W$ responsivity. V_π varying from 1 V [27] to 14.4 V [28]

Lastly, the down-conversion process contains inefficiencies. This inefficiency is manifested within the responsivity of the photodetector, r_{PD} , given in A/W . This metric represents the quantum efficiency, conversion efficiency of photons to electrons, as well as the photon energy and electron energy. Responsivity exhibits wavelength dependency because the photon energy above the band gap of the photodetector is energy that is not captured in this detection method [9]. A typical responsivity of an off-chip photodetector is $0.75 A/W$ [1], while on-chip germanium-on-silicon photodetectors can exhibit a responsivity of $1.09 A/W$. Recently, work on Avalanche photodiode (APD) detectors integrated on a silicon platform has shown even higher responsivities with increasing bandwidths [29] resulting in 5-10 dB of link gain [30]. APDs accelerate generated

electron-hole pairs with maximum reverse bias voltage causing collisions which result in additional electron-hole pair generation.

$$G_{Detect} = r_{PD} \quad (1.7)$$

In addition to the loss due to inefficiency of up-conversion and down-conversion, the modulated optical carrier is attenuated through the optical circuit. This attenuation includes guiding losses, coupling losses, and processing losses. Within a discrete system, depending on the processing tasks, this can typically be between 2-10 dB. The guiding loss within a microwave photonic systems is very small due to the low loss, $1\text{dB}/\text{Km}$, of single mode fiber (SMF) [9]. However, coupling loss can accumulate quickly, at 1dB per connector for COTS fiber connectors. This loss can be lowered in commercialized products via fiber splicing and polarization maintaining fibers. Discussed in following sections, the optical loss mechanisms due to guiding and coupling within a photonic integrated circuit are significantly more complex due to nonlinearities within the waveguide. The RF link loss due to optical guiding and circuitry loss is equivalent to the square of optical loss [16]. A change in optical power, ΔP_{opt} , results in a linear change in photocurrent, I_{ph} . A change in photocurrent results in a squared change in RF power, ΔP_{RF}^2 (eqn. 1.8).

$$\begin{aligned} \Delta P_{opt} &= \frac{\Delta I_{ph}}{r_{PD}} \\ \Delta P_{RF} &= \Delta I_{ph}^2 R_L \\ \sqrt{\frac{\Delta P_{RF}}{R_L}} &= \Delta P_{opt} r_{PD} \\ \therefore \Delta P_{RF} &\propto \Delta P_{opt}^2 \end{aligned} \quad (1.8)$$

The combination of the gain terms previously mentioned results in the link loss equations for a discrete implementation of a direct and external modulated microwave photonic link. The equations highlight which device parameters are critical for operation as well as design choices such as optical power which can impact the RF performance of the link.

$$G_{DM} = \frac{1}{4} s_{LD}^2 G_{opt}^2 r_{PD}^2 \quad (1.9)$$

$$G_{EM} = \frac{1}{4} \left(\frac{P_{opt} T_{Mod} R_L \pi}{2V_\pi} \right)^2 G_{opt}^2 r_{PD}^2 \quad (1.10)$$

1.3 Noise Figure of Microwave Photonic Link

The noise factor (F) of an RF system is defined as the degradation of signal-to-noise (SNR) due to the device-under-test (DUT). Mathematically, this is expressed by the ratio of the SNR into the DUT over the SNR after the DUT, eqn. 1.11. Noise figure (NF) is more commonly cited which is the logarithmic representation of the linear noise factor. The ratio of SNRs can be simplified by equating signal out equal to signal in multiplied by the gain of the system and then cancelling the like signal terms, 1.11. Therefore, the noise figure metric is dependent on link gain but additionally represents the noise generated by the DUT. The comprehensiveness of noise figure makes this a critical metric while evaluating and comparing RF systems, regardless of technological platform.

$$\begin{aligned} F &= \frac{SNR_{in}}{SNR_{out}} \\ NF &= 10 \log_{10}(F) \\ F &= \frac{\frac{S_{in}}{N_{in}}}{\frac{S_{out}}{N_{out}}} \\ F &= \frac{N_{out}}{GN_{in}} \end{aligned} \quad (1.11)$$

To begin calculating noise figure, the noise sources which impact the microwave photonic link must be identified and accounted for. There are three dominant noise terms within microwave photonic systems: thermal noise, shot noise, and laser relative intensity noise (RIN). These noise terms are modeled such as [5]; The noise terms are modeled as current sources which are wide-sense stationary, ergodic and independent of each other [20, 1]. These assumptions allow the total noise power to be a summation of individual noise sources.

Thermal noise, also known as Johnson-Nyquist noise, is the noise power generated by the random thermal agitation of electrical carriers within conductors. The noise power is independent of the applied voltage. Johnson and Nyquist presented the mean squared noise current due to thermal noise, eqn. 1.12 proportional to temperature, T , noise bandwidth Δf , and inversely proportional to resistance [1]. Additionally, this equation includes Boltzmann's constant, k . Thermal noise is a flat, 'white', noise source over the bandwidth of optoelectronic devices.

$$\langle i_{th}^2 \rangle = \frac{4kT\Delta f}{R} \quad (1.12)$$

There is thermal noise present at the input of the microwave photonic system, at the modulator or DML, as well as out of the system, at the photodetector. Therefore, the noise current due to thermal noise out of the microwave photonic link should be multiplied by a factor $(1 + G)$ to account for the thermal noise at the photodetector and the thermal noise from the modulator attenuated by the system [16]. Note, thermal noise is independent with respect to optical power.

Shot noise is noise power generated at the photodetector due to the statistical arrival of photonics from incident optical power on a photodetector. The statistical model for the distribution of incident photons is stationary Poisson random process with a white spectral density. This generated noise power is directly proportional to the electron charge, q , and the sum of the average generated photocurrent [6, 9] over the detection bandwidth, Δf . Within this analysis, the small transient of shot noise is considered negligible, and therefore, the noise can be treated as "white" [1]. Note, that this is the current at the photodetector, and therefore, to relate this to input optical power, the optical loss must be accounted for.

$$\langle i_{sh}^2 \rangle = 2q\langle i_{PD} \rangle \Delta f \quad (1.13)$$

The last primary noise source within the microwave photonic link is the relative intensity noise (RIN) of the laser. This metric accounts for multiple mechanisms which lead to intensity fluctuations of the optical source. Including spontaneous laser emission, which results in incoher-

ent light, the reflection selection of the laser facet, and the fluctuations in pump current [1]. The RIN of an optical source has a strong frequency dependency peaking at the relaxation oscillation frequency, typically kHz, of the laser cavity, followed by a roll-off equal to frequency squared, finally settling in a flat 'white' noise frequency region, Fig. 1.6. Therefore, within this analysis, calculations can be simplified by operating far above the relaxation oscillation frequency. Operating above this strong noise region allows for the elimination of the RIN frequency dependency [2]. Additionally, RIN is defined as a single-side power spectral density, instead of double-sided which allows for RIN to be limited to positive bandwidths reducing the bandwidth dependency from $2\Delta f$ to Δf [21]. Note, the RIN power has a square dependency on the optical power incident to the photodetector. Including optical amplifiers within the microwave photonic link leads to additional intensity noise from amplified spontaneous emission (ASE) which shares the same proportionality as RIN [2].

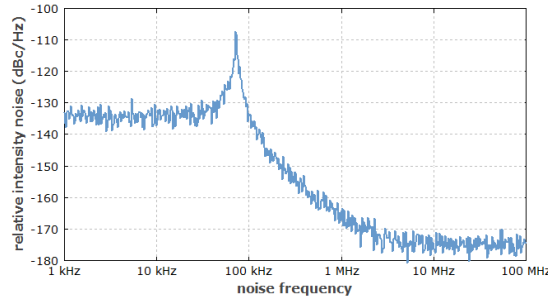


Figure 1.6: Example RIN frequency spectrum for commercial laser to understand different frequency regions. Source: https://www.rp-photonics.com/relative_intensity_noise.html

$$\langle i_{RIN}^2 \rangle = 10^{(RIN/10)} \langle i_{PD}^2 \rangle \Delta f \quad (1.14)$$

Therefore, the total noise current of the microwave photonic link is a summation of the thermal noise at the modulator and photodetector, the shot noise, and the RIN. This is shown in eqn. 1.15 and can be converted to noise power, N_{out} , and expanded within eqn. 1.16

$$\langle i_{Nout} \rangle = \frac{1}{2} (\langle i_{thmod} \rangle + \langle i_{sh} \rangle + \langle i_{RIN} \rangle + \langle i_{thPD} \rangle) N_{out} = \langle i_{Nout}^2 \rangle R_L \quad (1.15)$$

$$\begin{aligned}\langle N_{out} \rangle &= \frac{1}{4} \left((1 + G_{opt}) \langle i_{th}^2 \rangle + \langle i_{sh}^2 \rangle + \langle i_{RIN}^2 \rangle \right) \\ \langle N_{out} \rangle &= \frac{1}{4} \left((1 + G_{opt}) \frac{4kT\Delta f}{R} + 2q\langle i_{PD} \rangle \Delta f + 10^{(RIN/10)} \langle i_{PD}^2 \rangle \Delta f \right)\end{aligned}\quad (1.16)$$

The noise power into the system, N_{in} is defined by eqn. 1.17 with respect to the input thermal noise and resistive impedance matching.

$$N_{in} = kT\Delta f \quad (1.17)$$

Now that the gain terms and the noise terms for the two microwave photonic link architectures are defined, these terms can be substituted into the noise factor equation 1.11 which results in eqn. 1.18. Note, the bandwidth dependency of the noise sources are factored out due to the dependency on the input noise term and output noise terms.

$$F = 1 + \frac{1}{G} + \frac{qr_{PD}P_{PD}R_L}{2GkT} + \frac{P_{PD}^2 r_{PD}^2 R_L RIN}{4GkT} \quad (1.18)$$

Substituting in the gain terms for external and direct modulation yields architecture-specific noise figure terms, eqn. 1.19 and eqn. 1.20.

$$F_{DM} = 1 + \frac{4}{(s_{LD}G_{opt}r_{PD})^2} + \frac{2qP_{in}R_L}{s_{LD}^2 G_{opt}r_{PD}kT} + \frac{P_{in}^2 R_L RIN}{s_{LD}^2 kT} \quad (1.19)$$

$$F_{EM} = 1 + \frac{16V_\pi^2}{\pi^2 P_{in}^2 G_{opt}^2 r_{PD}^2 R_L^2} + \frac{16qV_\pi^2}{\pi^2 P_{in} G_{opt} r_{PD} R_L kT} + \frac{4V_\pi^2 RIN}{\pi^2 R_L kT} \quad (1.20)$$

The noise figure terms were simulated for a typical discrete microwave photonic link shown in Fig. 1.7. The simulated links were assumed to have 5 dB optical loss and 0.75 A/W responsivity. An MZM with a V_π of 5 V and a T_{mod} of 4 dB [31]. A DML with slope efficiency of 0.3761 A/W [26] and RIN of -162 dB/Hz. The optical source for the EM link was assumed to have a RIN of -160 dB/Hz. The simulation is swept from optical power of 0 dBm to 25 dBm. The directly modulated (DM) architecture has a 37 dB noise figure at 0 dBm. The directly modulated

(DM) architectures operate optimally with respect to noise figure at low optical powers. This optimal region is due to the gain of the link being independent of optical power yet two noise terms, shot and RIN, have optical power dependencies. Thus, by operating at low optical power, the DM link becomes thermal noise dominated, and noise power is minimized. Increasing optical power only results in increased noise, therefore increasing the noise figure. There are caveats to linearity by operating a directly modulated laser at too low optical powers, which will be explored in the dynamic range section. At 0 dBm, the DM link has a noise figure of 37 dB.

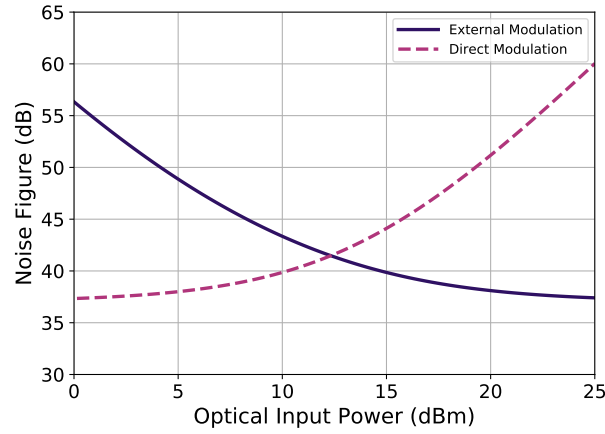


Figure 1.7: Noise figure verse optical power simulation for standard directly modulated link (pink dashed) and externally modulated link (purple solid).

The gain of the externally modulated (EM) architecture is dependent on the square of optical power. Therefore, within the thermal noise limited region, the noise figure of the link will be improved by the inverse square of optical power (1-2 dB per 1 dB increase in optical power). Within the shot noise limited region, the noise power scales linearly with optical power, and hence the improvement in noise figure is inversely proportional to optical power (1 dB per 1 dB increase in optical power). Lastly, when the EM link is RIN dominated, the signal power and noise power scale equally, leading the link to asymptotically reach a constant noise figure independent of optical power. The three noise regions and the respective derivative of noise figure verse optical power is shown in Fig. 1.8.

The optical power operating point in which different noise terms begin to dominate is

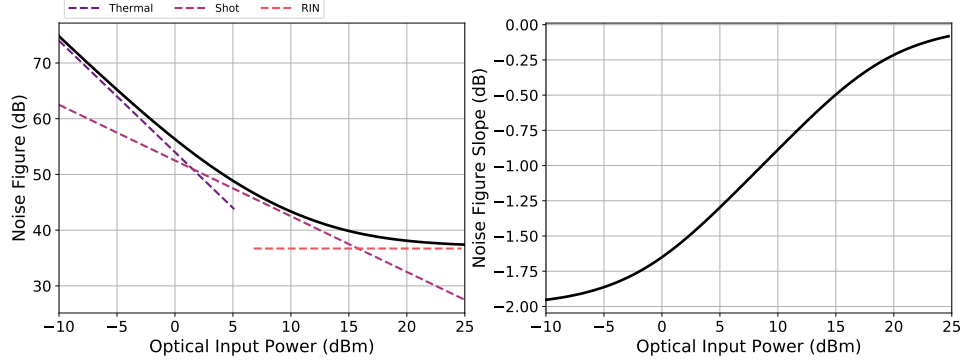


Figure 1.8: Noise figure verse optical power for external modulated link with highlighted noise regions (left). Derivative of noise figure verse optical power which analytically demonstrates the different noise regions (right).

dependent on the temperature that determines when the link transitions from thermal noise limited to shot noise limited. The link transition from shot noise limited to RIN limited is dependent on the RIN of the optical source. A high RIN of $-150\text{dB}/\text{Hz}$ could be representative of a low-cost solid-state laser or an integrated Multi-Quantum Well (MQW) Distributed Feedback Laser (DFB) [32]. Alternatively, a low RIN of $-165\text{ to }-170\text{dB}/\text{Hz}$ has been demonstrated using an extended-Distributed Bragg Reflector (DBR) laser [33, 34]. The DM and EM architectures were swept over these RINs to demonstrate how a highly noise optical source could dominate at relatively low optical powers. This sweep also demonstrates that the performance of the EM link is much more sensitive to RIN than DM links. This is due to the difference in optimal optical power operating points. Note, the EM architecture with lowest RIN stays within the shot noise limited region through 25 dBm optical power.

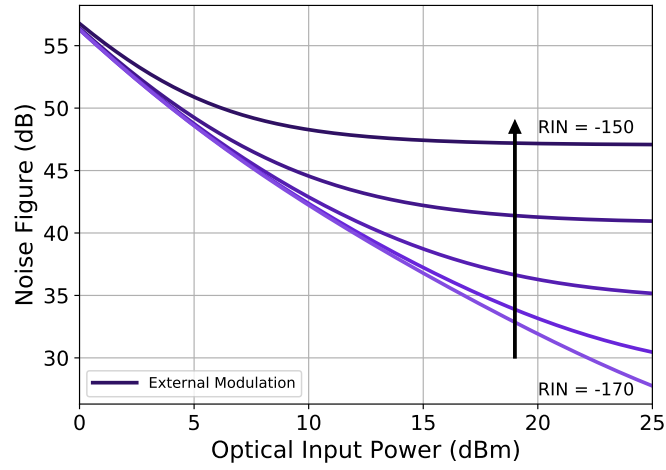


Figure 1.9: Noise figure verse optical power of a standard EM link with the RIN of the optical source swept from -170 dB/Hz [33, 34] to -150 dB/Hz [32].

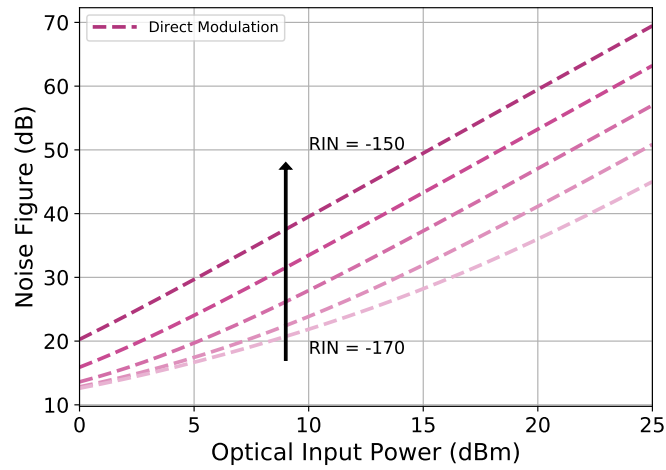


Figure 1.10: Noise figure verse optical power of a standard DM link with the RIN of the optical source swept from -170 dB/Hz [33, 34] to -150 dB/Hz [32].

1.4 Preamplification of Microwave Photonic Link

In recent years, the bandwidth performance of low noise amplifiers (LNA) has dramatically increased to match that of microwave photonic systems [35]. This improvement and the benefits of LNA implementation have led to the ubiquitous use of LNAs in microwave photonic systems. The Friis equation for noise, eqn. 1.21, defines the total noise factor of series RF systems. The idea of low noise amplification is to significantly amplify the signal gain in the RF chain before the introduction of optical noise. Considering that the microwave photonic systems developed for this thesis are intended to operate at the front-end of the RF chain, as shown by the Friis equation, the noise figure of those initial elements will limit the performance of the entire chain. Therefore, the performance of the LNA is critical to the overall effectiveness of the microwave photonic system. Assuming that the LNA does not bandwidth limit the optical system, the caveats of pre-amplification will be further explored within the dynamic range analysis.

$$F_{Total} = F_1 + \frac{F_2 - 1}{G_1} + \frac{F_3 - 1}{G_1 G_2} + \dots + \frac{F_N - 1}{G_1 G_2 \dots G_{N-1}} \quad (1.21)$$
$$F_{MPC+LNA} = F_{LNA} + \frac{F_{MPC} - 1}{G_{LNA}}$$

The combined link gain of the microwave photonic system with preamplification will simply increase by the gain of the LNA. The overall noise figure will be improved by a factor determined by the Friis equation. The improvement of the noise figure is shown in Fig. 1.11. In this simulation, the previously defined standard EM and DM links were preamplified by an LNA with gain 23 dB and noise figure 4 dB and bandwidth of 54 GHz (Model Number: RLNA05M54GA). This improved the noise figure of the DM and EM link to 7.5 dB and 14.8 dB, respectively. An improvement of 20.4 dB and 22.6 dB, respectively.

To further explore the effect of the LNA metrics on the microwave photonic link, the gain and noise figure was swept in Fig. 1.12 and 1.13. The noise figure of the combined link is inversely proportional to the gain of the amplifier, but saturates at the noise figure of the LNA as shown in the DM architecture in Fig. 1.12. Therefore, when considering the required gain of the LNA, consider

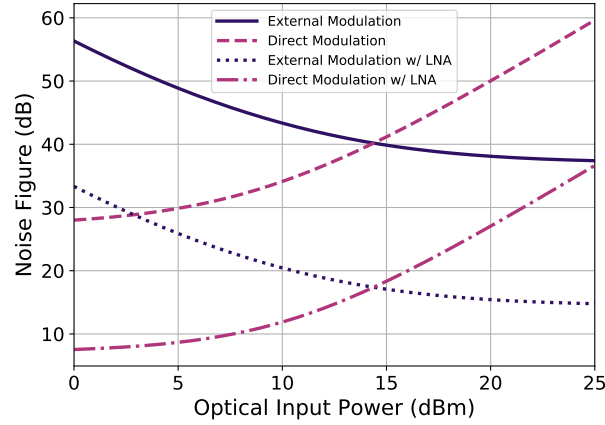


Figure 1.11: Noise figure verse optical power for DM and EM links with inclusion of low noise amplification (dashed). The simulated amplifier has a gain of 23 dB and noise figure of 4 dB.

the difference in the NF of the microwave photonic link and the noise figure of the LNA. This relationship holds true inversely while considering sweeping the noise figure. If the noise figure of the LNA is close to the combined noise figure of the LNA and microwave photonic link given the LNA gain, reducing the noise figure of the LNA will result in a reduction of the combined link. This effect is shown with respect to the DM link in Fig. 1.13. Although if the combined noise figure of the LNA and microwave photonic link is significantly above the noise figure of the LNA, reducing the noise figure of the LNA will not significantly improve the link.

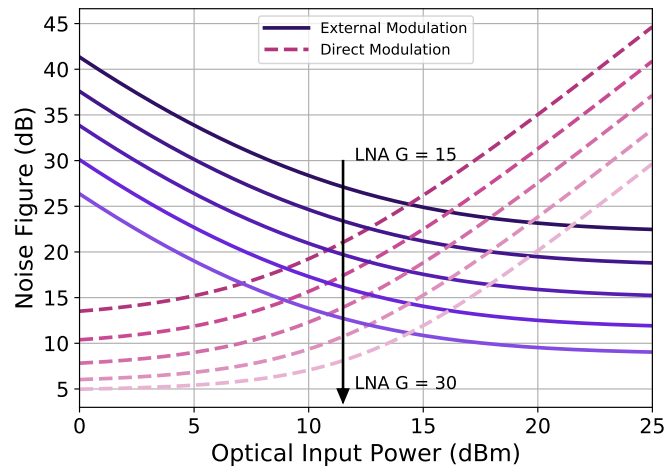


Figure 1.12: Noise figure verse optical power for DM and EM links with varying LNA gain from 15 dB to 30 dB with fixed noise figure of 4 dB.

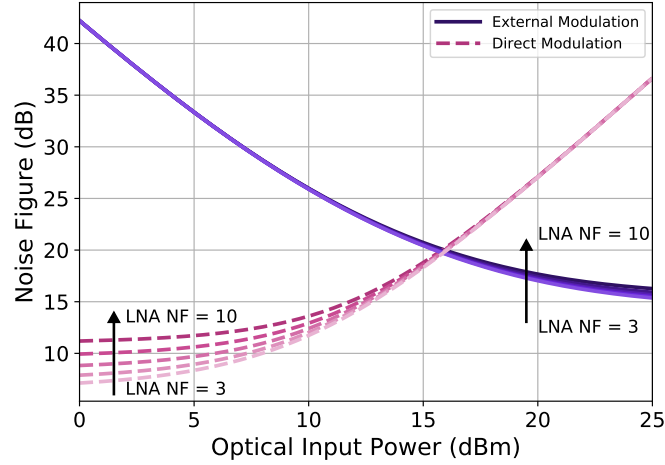


Figure 1.13: Noise figure verse optical power for DM and EM links with varying LNA NF from 3 dB to 10 dB with fixed gain of 23 dB.

1.5 Silicon Photonic Loss Mechanisms

Within this section, the analysis will be extended to include the loss mechanisms due to silicon integration. Monolithic integration can offer a reduction in loss due to the elimination of the need to couple between each optical element. This advantage can be negated on the basis of linear and nonlinear losses within the silicon waveguide and processing elements, which has dependency on optical operating power and optical circuitry.

Specific to silicon photonics, optical coupling of the laser source to the photonic integrated circuit (PIC) is required due to an inability of silicon to lase. Silicon being an indirect band gap material [36]. The coupling from the laser source to the silicon photonic integrated chip (PIC) has significantly improved in recent years and is heavily researched [37, 38]. The two primary commercial-grade methods for optical coupling to chip are edge coupling or vertical grating coupling. Edge coupling offers the lower of the two in terms of insertion loss, typical 1.5 dB [37], but requires submicrometer alignment precision [36]. Vertical coupling through grating couplers increases the alignment tolerance to micrometers, but reduces the coupling efficiency to between 3-4 dB [37]. More advanced coupling techniques are being developed including photonic wire bonds, photonics plugs, and evanescent coupling with polymer waveguides. These new techniques can greatly relax alignment tolerances and improve coupling efficiencies, but are currently incom-

patible with commercial foundries, requiring custom processes and new materials [37].

1.5.1 Linear and Nonlinear Waveguide Loss

In addition to losses due to coupling inefficiencies, guiding on a silicon platform incurs more losses than guiding within a fiber-based system. With a compact fiber-based microwave photonic system, linear propagation loss can often be considered negligible, based on the system using a meter or less of fiber with a propagation loss of 1 dB per km [2]. A silicon photonic waveguide is considerably more lossy due to sidewall scattering, material losses within doped waveguides, metal absorption (if within 600 nm of the waveguide), and surface-state absorption due to improper waveguide passivation [36]. Photonic foundries can achieve a straight waveguide propagation loss, α_0 , of 1.04 dB/cm [39]. Bending the waveguide can lead to additional losses from the optical mode leaving the center of the waveguide, resulting in mode mismatch losses as well as radiative losses from stronger interaction with sidewall roughness. The expected loss for a standard $500 \times 220 \mu\text{m}$ strip waveguide is 0.01 dB per 90° turn if maintaining a bend radius $> 5 \mu\text{m}$ [36].

In addition to propagation loss, a silicon waveguide exhibits nonlinear optical loss mechanisms, Free Carrier Absorption (FCA) [40, 41] and Two-Photon Absorption (TPA) [7]. The nonlinear effects computed for this analysis were with respect to a standard 500 nm silicon-on-insulator strip waveguide.

Free carrier absorption is the transfer of photon energy to a free electron in the conduction band or a free hole in the valence band of a semiconductor [42]. The excited free carrier transitions states, and the photon energy is converted. The rate of this phenomenon is dependent on the band gap structure of the semiconductor, which determines the requirement of additional phonons for momentum conservation. The FCA coefficient is given by eqn. 1.22 [42]. Where, N is the concentration of free carriers, λ is the wavelength, q is the fundamental charge, ϵ_o is the vacuum permittivity, m_c is the conductivity effective mass of the free carrier, c is the speed of light, n is the refractive index, and τ is the mean time between collisions. This can be simplified by substituting silicon-specific coefficients and carrier-specific coefficients, resulting in eqn. 1.23.

Where ΔN_e is the concentration of free electrons and ΔN_h is the concentration of free holes [43]. In addition to the free-carrier concentration dependency, FCA is also dependent on the optical power density within the waveguide because for the process to occur a photon and free-carrier must be present. The FCA coefficient for silicon, σ_{FCA} multiplied by the carrier lifetime for silicon, τ_c , is 24.8 cm/GW [8, 7]. Note, there is also free-carrier dispersion (FCD) which does not impact optical loss but may impact the performance of phase sensitive optical circuitry.

$$\alpha_{FCA} = \frac{N\lambda^2 q^2}{4\pi^2 \epsilon_o m_c c^3 n \tau} \quad (1.22)$$

$$G_{FCA} = 8.5 * 10^{-18} \Delta N_e + 6.0 * 10^{-18} \Delta N_h \quad (1.23)$$

Two-photon absorption occurs when two photons within the waveguide are absorbed simultaneously, generating an electron-hole pair with energy equal to the sum of the energy of the two photons. The rate of this nonlinear process is dependent on the optical power density within the waveguide [44]. There are higher order multi-photon absorption mechanisms but they occur at much lower rates. TPA is dependent on the semiconductor material properties of the waveguide and is strongly dependent on the optical power density within the waveguide [44, 7]. The TPA coefficient for silicon, β_{TPA} is $9.71 * 10^{-27} \text{ cm}^2 \text{ s}$.

The nonlinear absorption effects of FCA and TPA can be combined into a single ordinary differential equation, eqn. 1.24. This equation allows for calculation of the power loss along the z-axis of the silicon waveguide. The first term is simply the linear propagation loss. The first nonlinear term is proportional to the optical power into the waveguide. The coefficient, α_2 , is defined as linear dependency component of TPA, eqn. 1.25. This is the TPA coefficient divided by the effective area. The effective area is determined by the integral of the square root of the cross-sectional optical power density squared divided by the integral of the spectral power density within the core to the power of four. The third term within the ordinary differential equation, α_3 , is dependent the square optical dependencies of FCA and TPA combined, eqn. 1.26. The coefficients

for TPA and FCA multiplied by free-carrier lifetime and divided by two times the photon energy multiplied by the effective area squared. For a standard silicon waveguide operating with transverse electric optical guiding mode (TE), α_2 is $32.6 \text{ cm}^{-1}\text{W}^{-1}$ and α_3 is $2,040 \text{ cm}^{-1}\text{W}^{-2}$ [8, 43, 7].

$$\frac{\delta P}{\delta z} = -\alpha_o P - \alpha_2 P^2 - \alpha_3 P^3 \quad (1.24)$$

$$\alpha_2 = \frac{\beta_{TPA}}{Area_{TPA}} \quad (1.25)$$

$$Area_{TPA} = \left(\int PD_{opt}(x, y)^2 dx dy \right)^2 / \int_{core} PD_{opt}(x, y)^4 dx dy$$

$$\alpha_3 = \frac{\beta_{TPA} \sigma_{FCA} \tau_c}{2 * h\nu Area_{eff}^2} \quad (1.26)$$

$$Area_{eff}^2 = \left(\int PD_{opt}(x, y)^2 dx dy \right)^3 / \int_{core} PD_{opt}(x, y)^6 dx dy$$

The inclusion of silicon photonic linear and nonlinear waveguide loss leads to the general link loss equation 1.27. The optical waveguide loss as a function of silicon waveguide length is shown for different optical powers into the waveguide in Fig. 1.14 (left). The simulation shows the significant nonlinear absorption of high optical powers within the first 100s of microns of the waveguide. After attenuation of the optical power to $< 10 \text{ dBm}$ optical power, the attenuation of the optical signal returns to the linear loss of the waveguide. This is shown analytically by simulating the loss for a 1 mm silicon waveguide as a function of the optical input power, Fig. 1.14 (right). This simulation demonstrates the optical power into the waveguide when nonlinear loss begins to dominate. Lengthening the waveguide in the simulation will not show much additional information as shown in Fig. 1.14 (left), the excess optical power above this nonlinear operating point is absorbed in the first 400 microns.

$$G_{RF} = (G_{Impedance})^2 (G_{mod})^2 (G_{opt})^2 (G_{Waveguide})^2 (G_{Detect})^2 \quad (1.27)$$

The additional loss mechanisms from the silicon waveguide are included in the link loss and noise figure for both DM and EM silicon photonic link architectures in Fig. 1.15. The inclusion

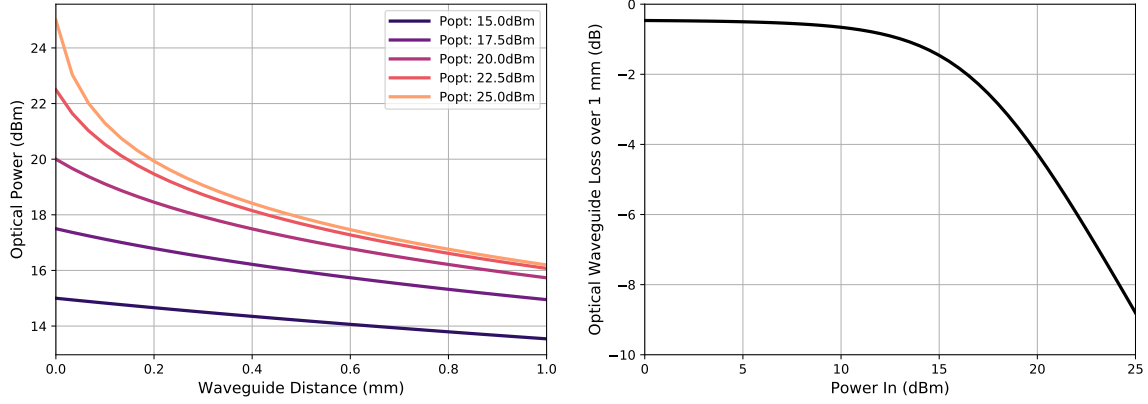


Figure 1.14: Optical power within the waveguide as a function of distance within the waveguide for varying optical powers. Analyzing the slopes of the attenuation provides information of the dominating loss mechanism linear or nonlinear (left). Optical loss as a function of optical power in for a 1 mm long silicon waveguide (right).

of the nonlinear loss terms which have linear and square proportionality to optical power leads to a limit to the gain of the EM link once optical loss equates to optical gain around 20 dB optical power. For the DM architecture, the additional loss at high optical power only further dissuades the design from operating this architectural type at high optical powers. With respect to noise figure, the EM architecture reaches a constant noise figure as a function of optical power at a lower input power compared to that of the discrete system. The silicon photonic links demonstrated a link loss of -27 dB and -25.2 dB, as well as an NF of 21.8 dB and 38.4 dB, for the DM and EM link type, respectively.

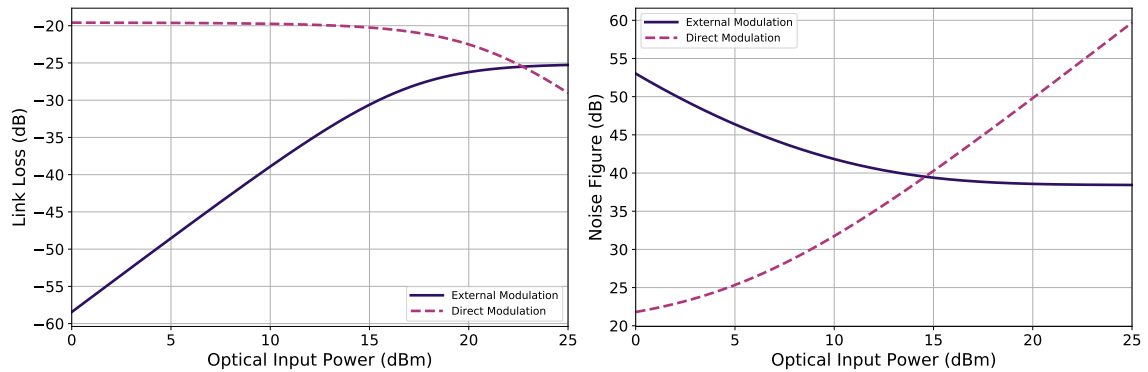


Figure 1.15: Link loss (left) and noise figure (right) as a function of optical power for a directly modulated and externally modulated silicon photonic link with waveguide length of 2 mm.

1.5.2 Nonlinear Microring Resonator Loss

As discussed in the previous section, the strength of the nonlinear loss from TPA and FCA is strongly dependent on the intensity of light within the silicon waveguide. Silicon PICs that implement resonator-based devices, such as microring resonators (MRR) used throughout the research presented in this thesis, result in significant optical power buildup [45]. The power buildup factor within an MRR, B , can significantly scale the optical intensity within the waveguide over the optical path length of the ring. For the simulations within this section, a B of 17.3 is used [46]. The power buildup factor, shown in eqn. 1.28, is dependent on the ratio of power remaining after one round-trip loss, a , the coupling ratio, r , and the detuning of the MRR, ϕ [45]. This power buildup as a function of MRR detuning is shown in Fig. 1.16.

$$B = \frac{a^2(1 - r^2)}{1 - 2\arccos(\phi) + a^2r^2} \quad (1.28)$$

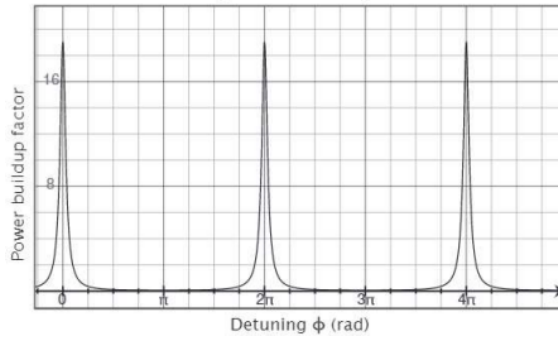


Figure 1.16: Power buildup within a microring resonator (MRR) as function of detuning for $r = 0.9$ and $a = 0.99$. From source: [45].

Fig. 1.17 (left) simulates the linear and nonlinear power loss within an MRR with radius of 15 microns. While 20 dBm is the maximum power put into the ring, the power buildup within the ring results in a built-up intensity maximum of 30.98 dBm. This power buildup in the ring brings the optical power close to the upper threshold, 33 of power handling, 33 dBm, within a silicon waveguide [47]. Fig. 1.17 (left) highlights the optical power loss as a function of optical power in for the 15 micron MRR compared to the 1 mm waveguide loss. Surprisingly, given that the optical

path length of the MRR is only 94 microns, the nonlinear loss due to the buildup adds significantly more loss than that of the waveguide. The point in which nonlinearities begin to dominate is shifted to the left by a factor of the buildup power within the microring. This phenomenon is shown clearly in Fig. 1.18, which simulates optical loss as a function of input power while sweeping the MRR buildup factor from a high quality factor ring, $B = 40$, to a low quality factor ring, $Q = 4.74$ [48].

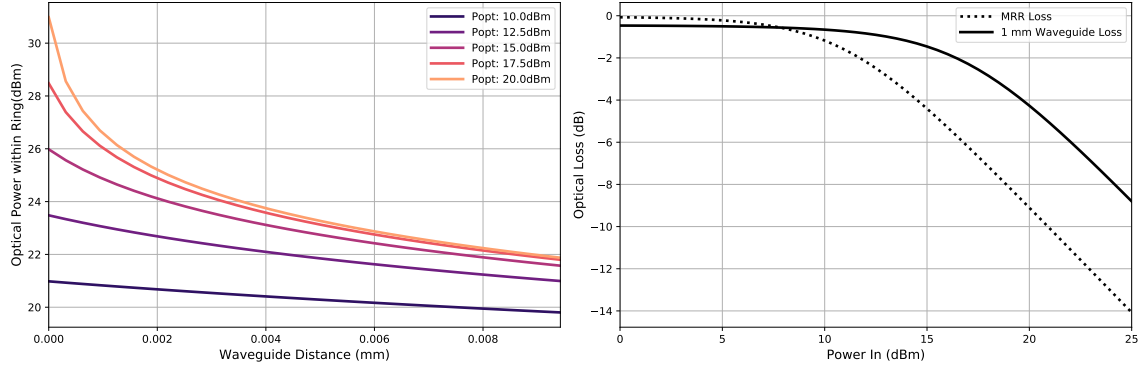


Figure 1.17: Optical power as a function of waveguide distances for varying optical powers, 10 dBm to 20 dBm, within a 15 micron radius microring resonator with buildup factor of 17.3 (left). Optical power loss as function of optical power in for microring resonator compared to 1 mm long waveguide (right).

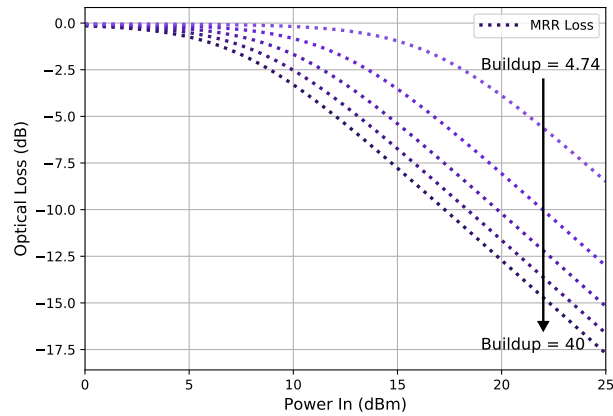


Figure 1.18: Optical linear and nonlinear loss of 15 micron microring with varying buildup factor from 40 to 4.3 as a function of optical power in.

The nonlinearity within the MRR is added to the generalized link loss equation for silicon photonic systems with resonator-based devices, resulting in eqn. 1.29. The results of FCA and

TPA within the MRR are shown in Fig. 1.19. The inclusion of nonlinear loss mechanism within the RF analysis yields the very interesting result of optimal optical power operating points. In the discrete microwave photonic system, the nonlinearity within single mode fibers is very low. Therefore, with sufficiently low RIN for an externally modulated system, the higher the optical power handling capabilities of optical components, modulator and photodetector, the better the RF components. For a silicon photonic integrated circuit without resonator devices, the analysis resulted in an optimal optical power operating point, which once reached the RF performance would reach a steady state. At this operating region, the system is relatively noise dominated, and therefore, the signal power and noise power are attenuated equally until nonlinear loss mechanisms are no longer strong. With resonator-based devices in the optical link, an optimal optical operating point can be clearly defined because operating above this point can lead to excess optical loss in the resonator, which would not normally be seen in the waveguide. For the 15 micron radius MRR with power buildup of 17.3, this results in an optimal point for gain and noise figure at 15 dBm input optical power. The optimal link loss and noise figure for the DM silicon photonic link was simulated to be -23.9 dB and 25.4 dB, respectively. The optimal link loss and noise figure for the DM silicon photonic link was simulated to be -33.7 and 40.1 dB, respectively.

$$G_{RF} = (G_{Impedance})^2 (G_{mod})^2 (G_{opt})^2 (G_{Waveguide})^2 (G_{MRR})^2 (G_{Detect})^2 \quad (1.29)$$

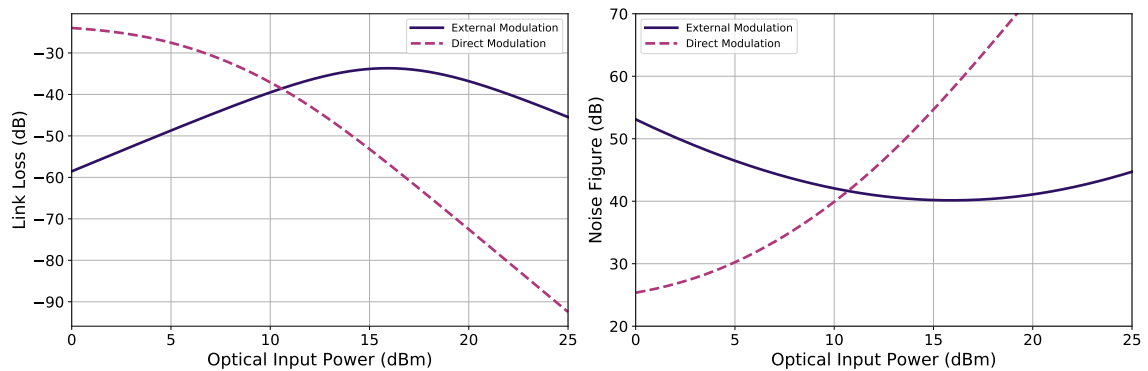


Figure 1.19: Link loss (left) and noise figure (right) as a function of optical input power for both DM and EM silicon photonic links with a 15 micron radius microring resonator with a buildup factor of 17.3.

Fig. 1.20 demonstrates the effect on RF performance by sweeping the buildup factor of the resonator-based device from 40 to 4.3. The RF performance degrades proportionally to the buildup factor, and the optimal optical input power shifts to lower powers as the buildup increases. The EM architecture is much more sensitive to the effects of nonlinearity due to performance dependency with high power operation. The DM architecture favors low optical power operation and is less sensitive to the nonlinear loss mechanisms.

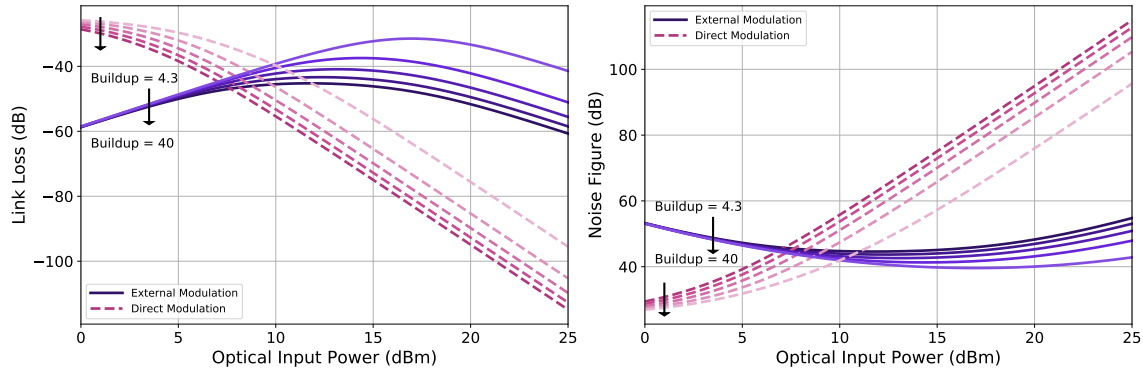


Figure 1.20: Link loss (left) and noise figure (right) as a function of input optical power for a silicon photonic circuit with microring resonators. The buildup factor is swept from 4.3 to 40. Representing low and high quality factor rings.

1.6 Spurious-Free Dynamic Range

The spurious-free dynamic range (SFDR) defines the range of powers which an RF system can process. The lower limit, defined as the minimal detectable signal (MDS), is the thermal noise floor plus the noise figure of the system. Any signal below this level will be degraded by the performance of the microwave photonic link and will be submerged under the noise floor. The upper limit to SFDR is defined relative to the order, n , of nonlinear signal within the RF system. The nonlinear signals generated are harmonics or intermodulation distortion products (IMD). Harmonics are integer multiples of the fundamental frequency, whereas IMDs are sum and difference frequencies. Within a microwave photonic system, the difficult IMD is the third-order IMD, this is because the beating of optical carriers centered at 193 THz results in a second order

harmonic centered at 386 THz, far outside the transmission window of the silicon waveguide. The third-order intermods, $2\omega_1 - \omega_2$ and $2\omega_2 - \omega_1$, fall close to the fundamental signals, only separated by the difference in fundamental frequencies. Hence, the upper limit is set to the input RF power at which the power of the IMDs exceeds the fundamental signals. Mathematically, the RF input and RF output point where the IMDs are equal power to the fundamental signals is called the n th-order input/output intercept point, IIP_n and OIP_n . $SFDR_n$ can be defined with respect to IIP_n as in eqn. 1.31 or with respect to OIP_n as in eqn. 1.32. This relationship is shown graphically in Fig. 1.21. For both the DM and the EM link architectures, operating under the assumptions presented in this analysis, specifically the quadrature operation of the MZM, the third-order IMD dominates [2, 5, 1].

$$MDS = NF + N_{floor} = NF + 174 \quad (1.30)$$

$$\begin{aligned} SFDR_n &= \frac{n-1}{n} (IIP_n - MDS) \\ SFDR_3 &= \frac{2}{3} (IIP_3 - NF + 174) \end{aligned} \quad (1.31)$$

$$\begin{aligned} SFDR_n &= \frac{n-1}{n} (OIP_n - MDS) \\ SFDR_3 &= \frac{2}{3} (OIP_3 - G - NF + 174) \end{aligned} \quad (1.32)$$

$SFDR_n$ is either presented with respect to per unit $Hz^{\frac{n-1}{n}}$ or with respect to a given bandwidth, Δf . Equation 1.33 allows for conversion between these two definitions.

$$SFDR_n(\Delta f Hz) = SFDR_n(1Hz) - \frac{n-1}{n} 10 \log_{10}(\Delta f) \quad (1.33)$$

Referring to the transfer function of the directly modulated laser, Fig. 1.3, there are two specific regions of operations where nonlinearities arise. At high current injection, the transfer function begins to compress, and the linearity of the slope is lost. At low currents when the bias current, I_{Bias} , is close to the threshold current for laser, $I_{threshold}$, the modulation of the link can

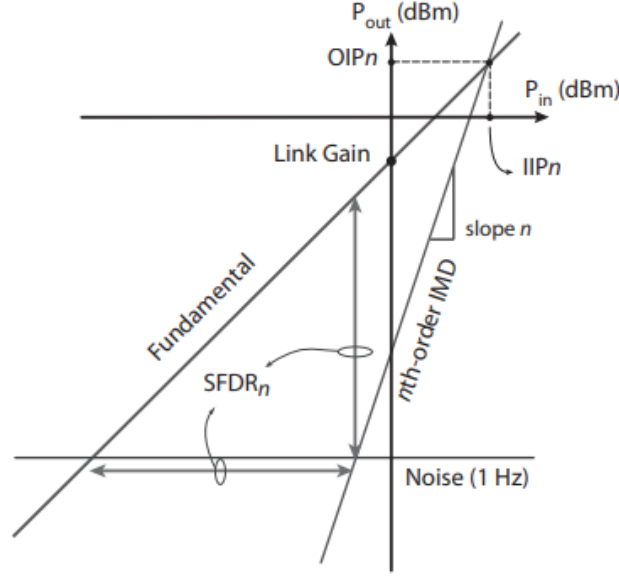


Figure 1.21: Graphical representation of spurious-free dynamic range. Source: [5]

experience clipping of high RF signals. Therefore, this modulation must be limited to small signals to avoid nonlinear distortion due to clipping [49, 50]. Mathematically, this requirement is defined in eqn. 1.35, where the difference in bias and threshold current must fulfill this inequality. Typically, a DM link will experience full linearity above 10 mW input power [50, 1]. There is research to use predistortion amplifiers to compensate for the nonlinearity introduced by clipping, but this will not be included within this analysis [51]. Combining these two nonlinear regions, results in eqn. 1.34, where the IIP_3 for a DML has a square dependency on optical power and an inverse proportionality with slope efficiency. The c_{DML} is the coefficient of the DML which describes the nonlinearities with the higher power regions. IIP_3 proportionality to optical power results in an increasing optimal operating point for the DM link type. The noise figure and therefore the MDS performs best at low optical powers but the linearity within this region is poor. Consequently, the optimal point with respect to dynamic is a trade-off between noise figure and linearity. For the silicon resonator-based DM link a $SFDR_3$ of $95.7 \text{ dB}/\text{Hz}^{2/3}$ was measured at 7.8 dBm optical power.

$$IIP3_{DM} = 10 * \log_{10} \left(\frac{c_{DML} * P_{opt}^2 * R_L}{2 * s_{LD}} \right) \quad (1.34)$$

$$I_m = m(I_{Bias} - I_{threshold})/2, 0 \leq m \leq 1 \quad (1.35)$$

The IIP3 of the interferometric modulator-based EM biased at quadrature is given by eqn. 1.36. Note that IIP_3 has a proportionality to V_π squared. As the modulator becomes less sensitive, the linear region at quadrature is stretched over a greater region of input RF power. Within the $SFDR_3$ calculations for an EM link, there are two competing terms with opposite proportionality to the sensitivity of the modulator. The lower limit of MDS improves as the noise figure decreases inversely proportional to the V_π squared while the upper limit of IIP_3 decreases proportionally to the V_π squared.

$$IIP3_{EM} = \frac{4V_\pi^2}{\pi^2 R_L} \quad (1.36)$$

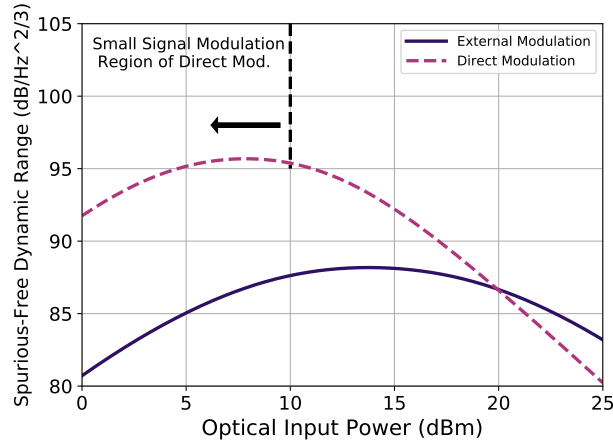


Figure 1.22: SFDR of directly modulated and externally modulated silicon photonic link with nonlinear loss as a function of optical power.

As discussed in earlier sections, preamplification can significantly reduce the noise figure of microwave photonic systems. With respect to SFDR, this reduction in noise figure significantly improves the minimal detectable signal. While, the lower limit is improved, the upper limit, IIP_3 ,

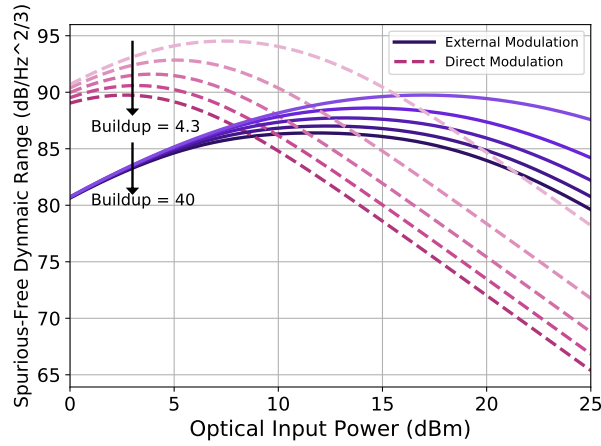


Figure 1.23: SFDR of directly modulated and externally modulated silicon photonic link as a function of optical power while sweeping the buildup factor of an MRR from 4.3 to 40.

is reduced by the gain of the low noise amplifier. The result of this trade-off is shown in Fig. 1.24 and Fig. 1.25 by sweeping the RF gain and noise figure of the LNA. The simulations show that the gain and noise figure of the LNA has an effect on the dynamic range of the link, but at optimal operating points the effect is much less significant than the preamplification improvements to noise figure.

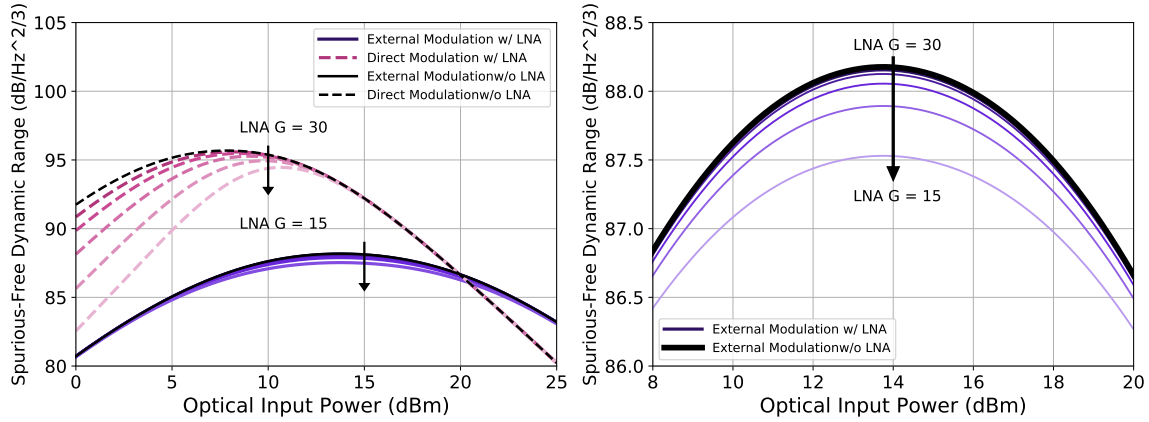


Figure 1.24: SFDR of DM and EM silicon photonic links with microring resonators as a function of optical power. Simulations include black curves with no preamplification and gain sweeps of the amplifier from 15 dB to 30 dB at a fixed 4 dB noise figure.

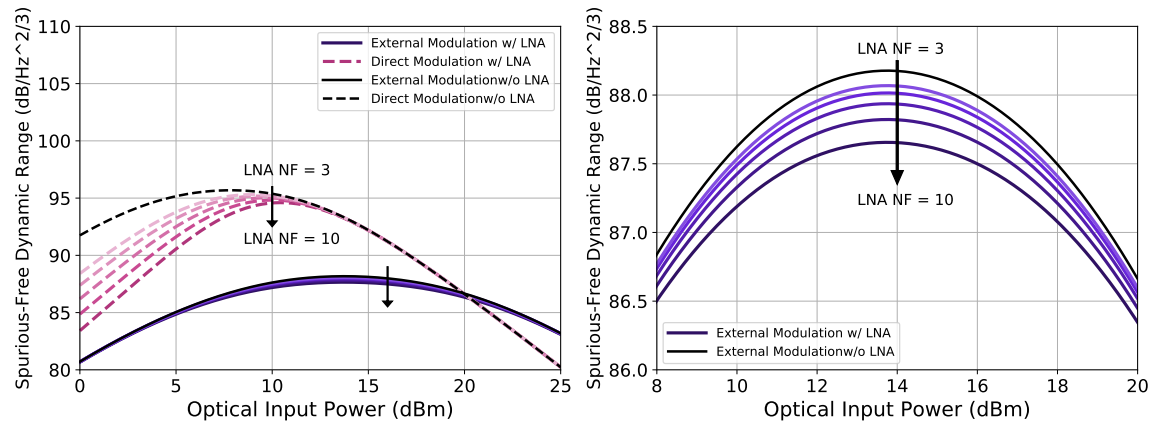


Figure 1.25: SFDR of DM and EM silicon photonic links with microring resonators as a function of optical power. Simulations include black curves with no preamplification and noise figure sweeps of the amplifier from 3 dB to 10 dB at a fix 23 dB gain.

Bibliography

- [1] C. H. Cox, *Analog optical links: theory and practice*. Cambridge University Press, 2006.
- [2] G. P. Agrawal, *Fiber-optic communication systems*. John Wiley & Sons, 2012.
- [3] V. J. Urick, K. J. Williams, and J. D. McKinney, *Fundamentals of microwave photonics*. John Wiley & Sons, 2015.
- [4] C. H. Cox, E. I. Ackerman, G. E. Betts, and J. L. Prince, “Limits on the performance of rf-over-fiber links and their impact on device design,” *IEEE Transactions on Microwave Theory and Techniques*, vol. 54, no. 2, pp. 906–920, 2006.
- [5] D. A. I. Marpaung, “High dynamic range analog photonic links: design and implementation,” *University of Twente*, 2009.
- [6] M. P. Chang, “A microwave photonic interference canceller architectures, systems, and integration,” *Princeton University*, 2017.
- [7] J. Bass, H. Tran, W. Du, R. Soref, and S.-Q. Yu, “Impact of nonlinear effects in si towards integrated microwave-photonic applications,” *Optics Express*, vol. 29, no. 19, pp. 30844–30856, 2021.
- [8] M. Tokushima, J. Ushida, and T. Nakamura, “Nonlinear loss characterization of continuous wave guiding in silicon wire waveguides,” *Applied Physics Express*, vol. 14, no. 12, p. 122008, 2021.

- [9] B. E. Saleh and M. C. Teich, *Fundamentals of photonics*. John Wiley & sons, 2019.
- [10] Y. Matsui, R. Schatz, D. Che, F. Khan, M. Kwakernaak, and T. Sudo, “Low-chirp isolator-free 65-ghz-bandwidth directly modulated lasers,” *Nature Photonics*, vol. 15, no. 1, pp. 59–63, 2021.
- [11] L. Ranno, P. Gupta, K. Gradkowski, R. Bernson, D. Weninger, S. Serna, A. M. Agarwal, L. C. Kimerling, J. Hu, and P. O’Brien, “Integrated photonics packaging: Challenges and opportunities,” *ACS Photonics*, vol. 9, no. 11, pp. 3467–3485, 2022.
- [12] A. J. Seeds and K. J. Williams, “Microwave photonics,” *Journal of lightwave technology*, vol. 24, no. 12, pp. 4628–4641, 2006.
- [13] R. Aguinaldo, A. Forencich, C. DeRose, A. Lentine, D. C. Trotter, Y. Fainman, G. Porter, G. Papen, and S. Mookherjea, “Wideband silicon-photonic thermo-optic switch in a wavelength-division multiplexed ring network,” *Optics Express*, vol. 22, no. 7, pp. 8205–8218, 2014.
- [14] J. Yao, “Microwave photonics,” *Journal of lightwave technology*, vol. 27, no. 3, pp. 314–335, 2009.
- [15] J. Capmany and D. Novak, “Microwave photonics combines two worlds,” *Nature photonics*, vol. 1, no. 6, p. 319, 2007.
- [16] C. H. Cox, E. I. Ackerman, G. E. Betts, and J. L. Prince, “Limits on the performance of rf-over-fiber links and their impact on device design,” *IEEE Transactions on Microwave Theory and Techniques*, vol. 54, no. 2, pp. 906–920, 2006.
- [17] R. Paschotta, “Optical heterodyne detection,” *RP Photonics Consulting GmbH papers*, 2012.
- [18] Y. Xing, S. Li, X. Xue, and X. Zheng, “Photonic-assisted rf self-interference cancellation based on optical spectrum processing,” *Journal of Lightwave Technology*, vol. 40, no. 7, pp. 2015–2022, 2021.

- [19] Y. Xing, S. Li, X. Chen, X. Xue, and X. Zheng, “Optical multi-tap rf canceller for in-band full-duplex wireless communication systems,” *IEEE Photonics Journal*, vol. 14, no. 5, pp. 1–7, 2022.
- [20] W. C. Van Etten, *Introduction to random signals and noise*. John Wiley & Sons, 2006.
- [21] D. A. I. Marpaung, “High dynamic range analog photonic links: design and implementation,” *University of Twente*, 2009.
- [22] M. Jahanbozorgi and S. E. Hosseini, “Effect of input impedance mismatch on the large-signal noise figure of microwave photonic links,” *OSA Continuum*, vol. 1, no. 2, pp. 564–572, 2018.
- [23] W. S. Chang, *RF photonic technology in optical fiber links*. Cambridge University Press, 2002.
- [24] P. A. Gamage, A. Nirmalathas, C. Lim, E. Wong, D. Novak, and R. Waterhouse, “Performance comparison of directly modulated vcsel and dfb lasers in wired-wireless networks,” *IEEE Photonics Technology Letters*, vol. 20, no. 24, pp. 2102–2104, 2008.
- [25] W. Sun, G. Zhao, Q. Lu, and W.-H. Guo, “High-speed directly modulated lasers based on high-order slotted surface gratings,” in *Physics and Simulation of Optoelectronic Devices XXV*, vol. 10098, pp. 166–171, SPIE, 2017.
- [26] APIC Corporation, *Highly Linear, Direct Modulated DFB Laser Module*, 3 2018. Rev. 1.
- [27] F. Eltes, C. Mai, D. Caimi, M. Kroh, Y. Popoff, G. Winzer, D. Petousi, S. Lischke, J. E. Ortmann, L. Czornomaz, L. Zimmermann, J. Fompeyrine, and S. Abel, “A batio₃-based electro-optic pockels modulator monolithically integrated on an advanced silicon photonics platform,” *Journal of Lightwave Technology*, vol. 37, no. 5, pp. 1456–1462, 2019.
- [28] A. Samani, M. Chagnon, D. Patel, V. Veerasubramanian, S. Ghosh, M. Osman, Q. Zhong, and D. V. Plant, “A low-voltage 35-ghz silicon photonic modulator-enabled 112-gb/s transmission system,” *IEEE Photonics Journal*, vol. 7, no. 3, pp. 1–13, 2015.

- [29] Y. Yuan, B. Tossoun, Z. Huang, X. Zeng, G. Kurczveil, M. Fiorentino, D. Liang, and R. G. Beausoleil, “Avalanche photodiodes on silicon photonics,” *Journal of Semiconductors*, vol. 43, no. 2, p. 021301, 2022.
- [30] M. Huang, S. Li, P. Cai, G. Hou, T.-I. Su, W. Chen, C.-y. Hong, and D. Pan, “Germanium on silicon avalanche photodiode,” *IEEE Journal of Selected Topics in Quantum Electronics*, vol. 24, no. 2, pp. 1–11, 2017.
- [31] EOSPACE, *High-Performance, Low-Vpi, 20GHz Small-Form-Factor Lithium Niobate Optical Modulator*, 9 2014. Rev. 1.
- [32] A. Leinse, K. Wörhoff, I. Visscher, A. Alippi, C. Taddei, R. Dekker, D. Geskus, R. Oldenbeuving, D. Geuzebroek, and C. Roeloffzen, “Hybrid interconnection of inp and triplex photonic integrated circuits for new module functionality,” in *Optical Interconnects XIX*, vol. 10924, pp. 37–46, SPIE, 2019.
- [33] Silvia M. Gentile, “Emcore releases high-power, ultra-low rin dwdm laser modules,” tech. rep., Marketwire, 2010.
- [34] P. A. Morton, C. Xiang, J. B. Khurgin, and J. E. Bowers, “Ultra-low noise semiconductor lasers,” in *2022 Conference on Lasers and Electro-Optics (CLEO)*, pp. 1–2, IEEE, 2022.
- [35] M. Božanić and S. Sinha, *Millimeter-wave low noise amplifiers*, vol. 164. Springer, 2018.
- [36] W. Bogaerts and L. Chrostowski, “Silicon photonics circuit design: methods, tools and challenges,” *Laser & Photonics Reviews*, vol. 12, no. 4, p. 1700237, 2018.
- [37] L. Ranno, P. Gupta, K. Gradkowski, R. Bernson, D. Weninger, S. Serna, A. M. Agarwal, L. C. Kimerling, J. Hu, and P. O’Brien, “Integrated photonics packaging: Challenges and opportunities,” *ACS Photonics*, vol. 9, no. 11, pp. 3467–3485, 2022.

- [38] L. Zimmermann, G. B. Preve, T. Tekin, T. Rosin, and K. Landles, “Packaging and assembly for integrated photonics—a review of the epixpack photonics packaging platform,” *IEEE Journal of Selected Topics in Quantum Electronics*, vol. 17, no. 3, pp. 645–651, 2010.
- [39] S. Y. Siew, B. Li, F. Gao, H. Y. Zheng, W. Zhang, P. Guo, S. W. Xie, A. Song, B. Dong, L. W. Luo, *et al.*, “Review of silicon photonics technology and platform development,” *Journal of Lightwave Technology*, vol. 39, no. 13, pp. 4374–4389, 2021.
- [40] R. Soref and B. Bennett, “Electrooptical effects in silicon,” *IEEE journal of quantum electronics*, vol. 23, no. 1, pp. 123–129, 1987.
- [41] G. T. Reed, G. Mashanovich, F. Y. Gardes, and D. Thomson, “Silicon optical modulators,” *Nature photonics*, vol. 4, no. 8, pp. 518–526, 2010.
- [42] S. C. Baker-Finch, K. R. McIntosh, D. Yan, K. C. Fong, and T. C. Kho, “Near-infrared free carrier absorption in heavily doped silicon,” *Journal of Applied Physics*, vol. 116, no. 6, p. 063106, 2014.
- [43] J. Bass, B. Brea, H. Tran, W. Du, R. Soref, and S.-Q. Yu, “The effect of two-photon absorption on the dynamic range of integrated microwave photonics links,” in *Silicon Photonics XV*, vol. 11285, pp. 216–223, SPIE, 2020.
- [44] E. W. Van Stryland, M. Woodall, H. Vanherzeele, and M. Soileau, “Energy band-gap dependence of two-photon absorption,” *Optics letters*, vol. 10, no. 10, pp. 490–492, 1985.
- [45] P. R. Prucnal and B. J. Shastri, *Neuromorphic photonics*. CRC press, 2017.
- [46] H. Jayatilaka, K. Murray, M. Á. Guillén-Torres, M. Caverley, R. Hu, N. A. Jaeger, L. Chrostowski, and S. Shekhar, “Wavelength tuning and stabilization of microring-based filters using silicon in-resonator photoconductive heaters,” *Optics express*, vol. 23, no. 19, pp. 25084–25097, 2015.

- [47] L. Zhang, Y. Li, Y. Hou, Y. Wang, M. Tao, B. Chen, Q. Na, Y. Li, Z. Zhi, X. Liu, *et al.*, “Investigation and demonstration of a high-power handling and large-range steering optical phased array chip,” *Optics Express*, vol. 29, no. 19, pp. 29755–29765, 2021.
- [48] E. C. Blow, S. Bilodeau, W. Zhang, and P. R. P. Thomas Ferreira de Lima, Josh Lederman, “Broadband radio-frequency performance demonstration, analysis, and optimization of silicon photonic neural networks,” *Advanced Photonic Research (Invited)*, 2023 (submitted).
- [49] R. Sabella, M. Paciotti, and A. Di Fonzo, “Impact of non-linear distortions on different modulation schemes in analog catv distribution systems,” in *Conference Proceedings LEOS’96 9th Annual Meeting IEEE Lasers and Electro-Optics Society*, vol. 2, pp. 406–407, IEEE, 1996.
- [50] S. A. Khwandah, J. P. Cosmas, I. A. Glover, P. I. Lazaridis, N. R. Prasad, and Z. D. Zaharis, “Direct and external intensity modulation in ofdm rof links,” *IEEE Photonics Journal*, vol. 7, no. 4, pp. 1–10, 2015.
- [51] C. Han, S.-H. Cho, M. Sung, H. S. Chung, and J. H. Lee, “Clipping distortion suppression of directly modulated multi-if-over-fiber mobile fronthaul links using shunt diode predistorter,” *ETRI Journal*, vol. 38, no. 2, pp. 227–234, 2016.